CANCER

# A bispecific glycopeptide spatiotemporally regulates tumor microenvironment for inhibiting bladder cancer recurrence

**Hong-Wei An[1,2]†, Da-Yong Hou[1,3,4]†, Jia Yang[1,2], Zi-Qi Wang[3,4], Man-Di Wang[1,2], Rui Zheng[1,2], Ni-Yuan Zhang[1,2], Xing-Jie Hu[1], Zhi-Jia Wang[1,3,4], Lu Wang[3,4], Di Liu[5], Jun-Feng Hao[5], Wanhai Xu[3,4]*, Yuliang Zhao[1,2,5]*, Hao Wang[1,2]***



**Up to 75% of bladder cancer patients suffer from recurrence due to postoperative tumor implantation. However, clinically used Bacillus Calmette-Guerin (BCG) treatment failed to inhibit the recurrence. Here, we report a bispecific glycopeptide (bsGP) that simultaneously targets CD206 on tumor-associated macrophages (TAMs) and CXCR4 on tumor cells. bsGP repolarizes protumoral M2-like TAMs to antitumor M1-like that mediated cytotoxicity and T cell recruitment. Meanwhile, bsGP is cleaved by the MMP-2 enzyme to form nanostructure for the long-term inhibition of CXCR4 downstream signaling, resulting in reduced tumor metastasis and promoted T cell infiltration. In orthotopic bladder tumor models, bsGP reduced the postoperative recurrence rate to 22%. In parallel, the recurrence rates of 89 and 78% were treated by doxycycline and BCG used in clinic, respectively. Mechanistic studies reveal that bsGP reduces the matrix microenvironment barrier, increasing the spatially redirected $CD8^+$ T cells to tumor cells. We envision that bis-targeting CD206 and CXCR4 may pave the way to inhibit tumor metastasis and recurrence.**

## INTRODUCTION

Nonmuscle invasive bladder cancer accounts for approximately 75% of patients with bladder cancer, which is mainly managed with transurethral resection of bladder tumor (*1*). However, one-third of patients still suffer from postoperative disease recurrence and carry a high risk of mortality due to postoperative tumor implantation (*2*). At present, postoperative instillation of chemotherapy drugs or Bacillus Calmette-Guerin (BCG) has been proven to reduce the recurrence rate of bladder cancer by destroying floating tumor cells (*3*, *4*). However, the postoperative recurrence rate still reaches 78% due to chemoresistance (*5*), and the immunosuppressive tumor microenvironment (TME) induces a poor response (*6*). The clinical results demonstrated that the strategy of neither inhibiting tumor cells alone nor regulating the tumor immunosuppressive TME alone achieved a satisfactory effect on inhibiting postoperative tumor implantation recurrence (*7*, *8*). Implantation recurrence of bladder cancer is caused by multiple factors, including redundant and synergistic effects among different pathways (*9*, *10*), which limits the effect of single-targeted therapy. Therefore, efforts to address these problems have become one of the major themes in the field of postoperative recurrence of bladder cancer.

Tumor progression is dependent not only on the characteristics of malignant cells but also on the behavior of the whole TME. The population of immune cells is an important player in tumor progression, including the process of metastasis. Currently, research shows that tissue-resident macrophages accumulate close to tumor cells early during tumor formation to promote epithelial-mesenchymal transition and invasiveness of tumor cells, inducing a potent regulatory T cell ($T_{reg}$) response that protects tumor cells from adaptive immunity (*11*, *12*). Moreover, repolarization of protumoral tumor-associated macrophages (M2-like TAMs) to an antitumor phenotype (M1-like) substantially reduced the numbers and altered the phenotype of $T_{regs}$, ultimately enhancing T cell recruitment into the tumor (*13*–*16*). In addition, T cell infiltration and circulation into tumors can be a key limiting factor for immunotherapy. However, tumor cells have formed a physical barrier that impedes T cell infiltration and access to the tumor tissue to prevent activity of anticancer immunity. Tumors contain a complex network of chemokines that control many of the basic properties of tumors, including immune cell recruitment, angiogenesis, and cell migration. CXCR4 has been shown to be highly expressed in various types of human cancers, including bladder cancer, breast cancer, pancreatic cancer, prostate cancer, and lung cancer (*17*–*19*), which is also essential for the invasive and metastatic properties (*20*–*22*). The application of plerixafor, a CXCR4 antagonist, in breast and pancreatic cancer has been demonstrated to substantially promote tumor apoptosis, reduce tumor metastasis, and selectively decrease intratumoral $T_{regs}$ (*23*, *24*). More evidence showed that inhibiting CXCL12/CXCR4 axis increased T cell infiltration in tumors and sensitized to anti-programmed death-ligand 1 and anti-cytotoxic T lymphocyte-associated antigen-4 antibodies therapy in pancreatic cancer (*23*). Thus, CXCR4 has become a very promising target for cancer therapy due to the inhibition of CXCR4 that not only reduced cell metastasis but also decreased

[1]CAS Key Laboratory for Biomedical Effects of Nanomaterials and Nanosafety, CAS Center for Excellence in Nanoscience, National Center for Nanoscience and Technology (NCNST), Beijing 100190, China. [2]Center of Materials Science and Optoelectronics Engineering, University of Chinese Academy of Sciences, Beijing 100049, China. [3]Department of Urology, The Fourth Hospital of Harbin Medical University, Heilongjiang Key Laboratory of Scientific Research in Urology, Harbin 150001, China. [4]NHC Key Laboratory of Molecular Probes and Targeted Diagnosis and Therapy, Harbin Medical University, Harbin 150001, China. [5]Core Facility for Protein Research, Institute of Boiphysics, Chinese Academy of Science, Beijing, China.
†These authors contributed equally to this work.
*Corresponding author. Email: xuwanhai@hrbmu.edu.cn (W.X.); zhaoyl@nanoctr.cn (Y.Z.); wanghao@nanoctr.cn (H.W.)

tumor fibrosis, facilitated T cell infiltration, and relieved immunosuppression (*23*, *24*).

Although pharmaceutical inhibitors and monoclonal antibodies (mAbs) have been developed for TAM-targeting or CXCR4-targeting treatments, their therapeutic efficacies have been greatly limited by the complex TME (*24*). In addition, the interactions of cancer cells with TAMs or with other immune cells are very complex, which substantially limits effectiveness of blocking one chosen cells′ activity (*25*). Progress in nanotechnology has provided a valuable opportunity for improving drug-loading/drug-releasing parameters, biocompatibilities, and drug circulation time (*26*, *27*). Notably, there are still some challenges for the development of effective targeting TAMs and CXCR4 biomaterials that regulate the interaction of multiple cells in transmission electron microscopy (TEM) temporally and spatially.

Here, we designed and performed a bispecific glycopeptide (bsGP) (CD206 × CXCR4) that simultaneously targets the CD206 receptor on M2-like TAMs and the CXCR4 receptor on bladder cancer cells (Fig. 1A). The modular molecular design included (i) mannose, as a TAM recognition and modulation molecule (*28*); (ii) LGASWHRPDK, as a tumor recognition motif, which could specifically bind CXCR4 (*29*); (iii) PLG$^{\downarrow}$YLG, as an enzyme-responsive peptide linker, which could be specifically cleaved by matrix metalloproteinase 2 (MMP-2) (*30*); and (iv) KLVFFAECG, as a self-assembly motif (*31*, *32*). In the TME, bsGP repolarized M2-like TAMs surrounding tumor cells to the M1 phenotype and then increased the recruitment of $CD8^+$ T cells, which were spatially redirected to tumor cells, resulting from remodeling of the immunosuppressive TME. In situ, bsGP is cleaved by MMP-2 to release the target CXCR4 residue, which spontaneously self-assembles into nanofibers (nano-GP) that specifically bind to CXCR4 in bladder cancer cells for long-term arrest of CXCR4 signaling, facilitating T cell infiltration through decreases tumor fibrosis. In orthotopic bladder tumor models, bsGP substantially reduced the postoperative recurrence rate to 22%, resulting from the increased frequencies of tumor-infiltrating $CD8^+$ T cells that were spatially redirected to tumor cells (Fig. 1A). We exploited innovative therapeutic concepts (CD206 × CXCR4) and unlocked functionalities of precise temporal and spatial control of the targets of CD206 and CXCR4 to efficiently suppress postoperative tumor implantation recurrence.

The goal of this study was to develop an anti-CD206/CXCR4 bsGP that would further overcome the immunosuppressive TME and increase the selectivity for targeting CXCR4-amplified tumor cells with high potency while sparing normal cells that express low amounts of CXCR4. Increased selectivity against CXCR4-amplified cells is expected to mitigate the risk of on-target off-tumor adverse effects and increase the therapeutic index of anti-CD206/CXCR4 bsGP. We anticipate that the developments of the innovative concepts described above will achieve optimal therapeutic efficacy.

## RESULTS

### Anti-CD206/CXCR4 bsGP rapidly targets tumor tissue

Initially, a bsGP [LGASWHRPDKK(PLGYLG-$(man)_3$-)LVFFAECG] (figs. S1 to S4) and a specific peptide for CXCR4 ($Pep_{CXCR4}$) (LGASWHRPDK) were synthesized as control molecules (fig. S5). The target CXCR4 residue nano-GP [LGASWHRPDKK(YLG)LVFFAECG] with the self-assembly sequence (fig. S6) and a bsGP [bsGPs with MMP-2 uncleavable linker (bsGP-uC)] [LGASWHRPDKK(PGSGSG-$(man)_3$)LVFFAECG] (fig. S7) were synthesized to elucidate the functions of the designed motifs and the self-assembled nanostructures. The details of the synthesis and molecular characterizations were provided in the Supplementary Materials. As shown in Fig. 1A, the operating principle of bsGP is that bsGP targeted CD206 and CXCR4 receptor, and the CXCR4-targeted residues released by MMP-2 hydrolysis can be assembled into nanofibers, further improving the affinity for CXCR4 receptor. All the experiments using human specimens were reviewed and approved by the Committees for Ethical Review of the Fourth Hospital of Harbin Medical University (2022-SCILLSC-33). After obtaining appropriate informed consent, we proved CXCR4 overexpression in tumor tissues of 15 patients with bladder cancer compared with that in normal tissues (fig. S8A), and then we selected two overexpressed cell lines, EJ and MB49-Luc bladder cancer cells, as model cells (fig. S8B). MMP-2 was demonstrated to be increased in the supernatant of EJ cells while absent in that of L929 cells according to the results of gelatin zymography analysis, which provided abundant enzyme to trigger the hydrolysis of bsGP (fig. S9) (*33*). Furthermore, the enzymatic responsiveness of bsGP molecules and the assembly behavior of released target-CXCR4 residues were verified. As the results of high-performance liquid chromatography (HPLC) (fig. S10), the peak of bsGP with a retention time (TR) of 14.0 min disappeared, and a new peak appeared [TR = 13.5 min, LGASWHRPDKK(YLG)LVFFAECG] after MMP-2 was added, demonstrating that bsGP {LGASWHRPDKK[PLG$^{\downarrow}$YLG-$(man)_3$]LVFFAECG} was specifically hydrolyzed by MMP-2. Next, as the released CXCR4-targeted residues self-assembled into nanofibers (nano-GP), the morphology self-assembly behavior of nano-GP was detected by atomic force microscopy (AFM) and TEM. According to the results of fig. S11, nano-GP presented typical well-ordered nanofibers with an average diameter of 20.9 ± 3.4 nm, and the height of the nanofibers was approximately 3.8 ± 0.2 nm by AFM imaging (Fig. 1, B and C). Furthermore, circular dichroism (CD) spectrometry and Fourier transform infrared (FTIR) spectroscopy were used to explore the self-assembled secondary structure of nano-GP (*34*). As shown in fig. S12, the negative signal at 199 nm in the CD spectra and the band at 1667 $cm^{-1}$ in the FTIR spectra imply the random coil structure of bsGP (*31*). In contrast, substantial changes were detected in the CD and FTIR spectra of nano-GP. The results showed that nano-GP had a β sheet conformation according to the positive peak at 195 nm and negative peak at 216 nm in the CD spectrum (fig. S12A) (*30*). In addition, the β sheet conformation of nano-GP was confirmed on the basis of the amide I band shifting from 1667 to 1630 $cm^{-1}$ in the FTIR spectra (fig. S12B) (*31*). After that, the evidently increased fluorescence of thioflavin T (ThT; a benzothiazole dye that exhibits enhanced fluorescence upon binding to amyloid fibrils) (*30*) further demonstrated the formation of a β sheet structure in nano-GP (fig. S13A). Representative fluorescent images of nano-GP showed that ThT fluorescence was well colocalized with stained β sheet structures of the nanofibers (fig. S13B). The ThT fluorescence was used to monitor the fibrillation of nano-GP in culture medium containing serum and phosphate-buffered saline (PBS) buffer (10 mM, pH 7.4) after 1, 4, and 12 hours. The results demonstrated that the assembly behavior of nano-GP in the culture medium containing

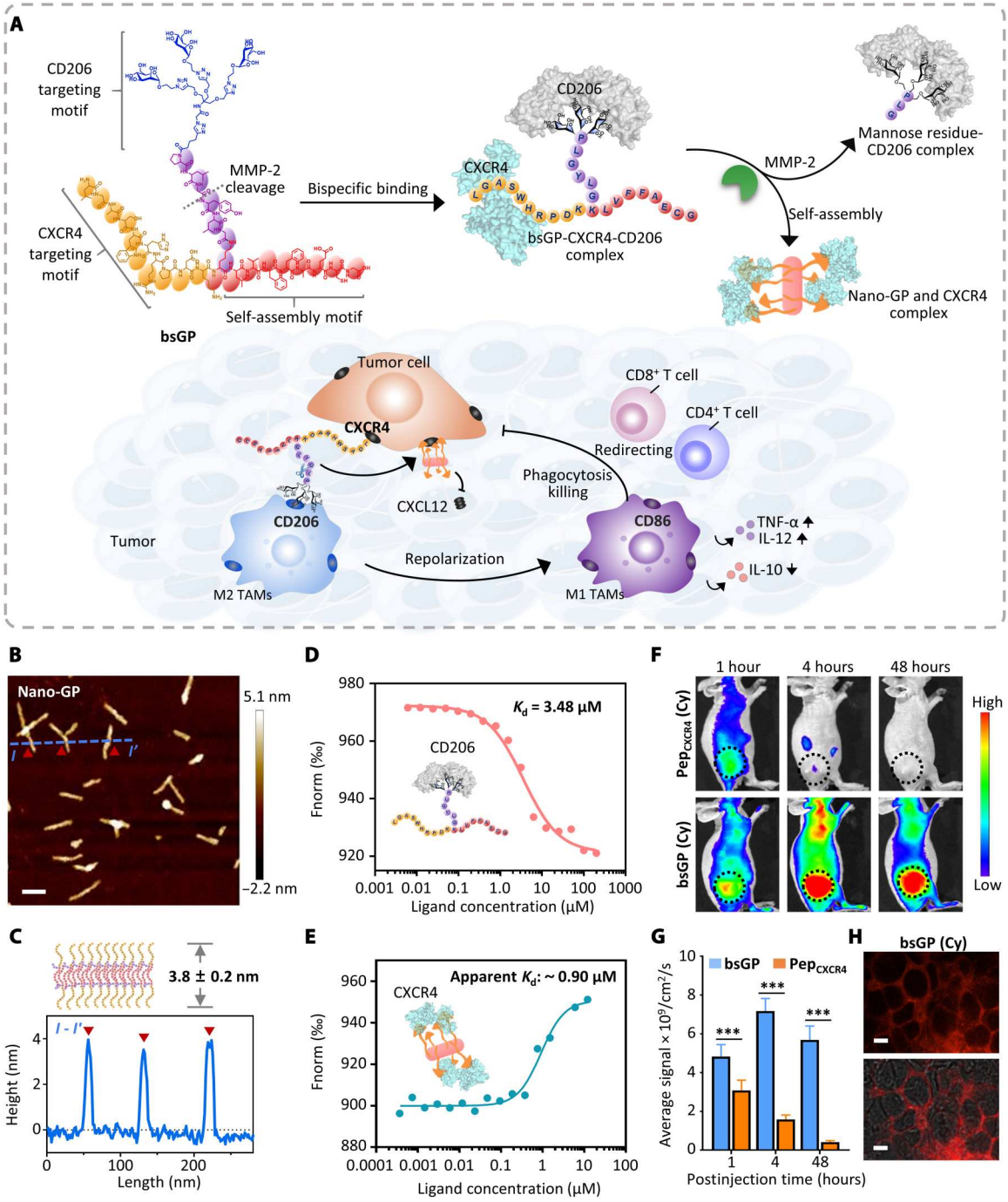


**Fig. 1. Application of bsGP to inhibit tumor recurrence.** Anti-CD206/CXCR4 bsGP specifically and rapidly targets tumor tissue. (**A**) bsGP (CD206 × CXCR4) was designed: (i) mannose, as a TAM recognition and modulation molecule; (ii) LGASWHRPDK, as a tumor recognition motif, which could specifically bind CXCR4; (iii) PLGYLG, as an enzyme-responsive peptide linker, which could be specifically cleaved by MMP-2; and (iv) KLVFFAECG, as a self-assembly motif. The bsGP specifically targets the CD206 receptor on protumoral M2-like TAMs and the CXCR4 receptor on bladder cancer cells for repolarizing M2-like TAMs surrounding tumor cells to an antitumor phenotype (M1-like) and long-term arrest of CXCR4 signaling. (**B**) Atomic force microscopy (AFM) images of self-assembled β sheet nanofibers of nano-GP. Scale bar, 50 nm. (**C**) AFM height images of the self-assembled nanofibers of nano-GP. (**D**) Microscale thermophoresis (MST) ligand binding measurements between bsGP and CD206. $K_d$ is the dissociation constant. (**E**) MST ligand binding measurements between nano-GP and CXCR4. (**F**) Representative near-infrared fluorescence images of Pep$_{CXCR4}$ (500 μM, 100 μl) and bsGP (500 μM, 100 μl) on EJ xenograft mice at 1, 4, and 48 hours after injection. The dotted circle points to the tumor tissue. (**G**) Quantitive fluorescence intensity in tumor (F) at 1, 4, and 48 hours after injection. (**H**) Representative fluorescence frozen sections images of the EJ tumor tissue after administration with bsGP. Scale bars, 5 μm.

serum was the same as that in PBS buffer (fig. S13, C and D). All the above results demonstrated that bsGP could be specifically cleaved by MMP-2 and spontaneously self-assembled into nanofibers with a β sheet conformation through intermolecular hydrogen bonds.

Subsequently, the bsGP (CD206 × CXCR4) was verified to simultaneously target the CD206 receptor on M2-like TAMs and the CXCR4 receptor on bladder cancer cells. As a result, the confocal imaging shown that red fluorescence [cyanine (Cy)-labled bsGP] was observed on the cytomembrane of tumor cells (EJ) and macrophages cells (RAW264.7) (fig. S14A). We constructed EJ cells expressing the green fluorescent protein–encoded CXCR4 receptor by plasmid transfection. Then, the pretransfected EJ cells were incubated with bsGP to observe the colocalization fluorescent signal by confocal laser scanning microscope (CLSM) imaging. Overlapping green fluorescence (CXCR4) with red fluorescence (bsGP) was observed on the cytomembrane of EJ cells (fig. S14B). In addition, the presence of a nanofibrillar network was observed on the surface of EJ cells treated with bsGP through scanning electron microscopy (SEM) (fig. S15A). In contrast, no nanofibrillar structure was detected on the surface of saline-treated cells (fig. S15B).

Furthermore, we tested the affinity of bsGP to the CD206 and CXCR4 receptor, respectively. This result suggests that three branched mannosides decorated bsGP with high affinity [dissociation rate constant ($K_d$), 3.48 μM] readily surpassed the affinity of mannose ($K_d$, ~1000 μM) by about 300-fold (Fig. 1D) (*35*). In addition, we also tested the binding of nano-GP to CXCR4 expressed on tumor cells. As a result, nano-GP showed a higher affinity for CXCR4 receptor (apparent $K_d$, ~0.90 μM) by the multivalent cooperative interactions than that of bsGP ($K_d$, 112 μM), further demonstrating that the self-assembled nanostructure sufficiently improved selectivity toward CXCR4 by the higher binding affinity (Fig. 1E and fig. S16) (*36*). Subsequently, EJ xenograft mice were built to further evaluate the specific targeting and persistence of bsGP in tumors through intravenous injection. Moreover, no substantial impact was observed on the viability of EJ and RAW264.7 cells after culture with $Pep_{CXCR4}$ or bsGP at a concentration of 50 μM (fig. S17). In vivo fluorescence images of tumor-bearing mice were obtained after treated with $Pep_{CXCR4}$ (500 μM, 100 μl) and bsGP (500 μM, 100 μl) (Fig. 1F). In vivo imaging data showed that bsGP could rapidly target to tumor tissue within 1 hour, and the accumulation reached the highest in 4 hours, which was nearly fourfold that of the single-targeted molecule $Pep_{CXCR4}$ (Fig. 1G). The signal-to-noise ratio was as high as 7.8-fold, which precisely delineated the tumor margin in accordance with the histology analysis results (fig. S18). The above results indicated that the dual-targeting performance of bsGP could improve the specificity of the drug. Meanwhile, the penetration efficiency of bsGP was further evaluated in the same tumor tissue with immunofluorescence. The results showed that bsGP (red fluorescence signal) was far away from the vessels (green fluorescence signal), indicating the deep penetration capability of bsGP compared with that of the antibody (fig. S19) (*31*). Compared with antibody, bsGP could be rapidly and efficiently accumulated in solid tumors by virtue of its small size. At the same time, as bsGP is transformed into nanofiber structure in situ (Fig. 1H), it could retain in the tumor tissue for a long time up to 48 hours, which can realize the long-term effect of the drug (*37*, *38*). All the results showed that simultaneous targeting of a high proportion of macrophages and tumor cells in tumor tissue resulted in rapid drug accumulation and improved the selectivity of tumor tissue, and the unique size advantage of glycopeptide-based bsGP enabled "fast in and slow out" in tumor tissue.

## Anti-CD206/CXCR4 bsGP targets tumor cell to inhibit tumor progression

We further validated the impacts of bsGP on the proliferation and migration capacity of human EJ cells with colony formation and Transwell assays. The results showed that the cell proliferation capacity of tumor cells was substantially decreased in the bsGP groups compared with the saline and $Pep_{CXCR4}$ groups (fig. S20). Furthermore, the migration capacity of tumor cells in the bsGP groups was evidently decreased compared with that in the saline and $Pep_{CXCR4}$ groups (fig. S21). This evidence demonstrated that bsGP could inhibit the proliferation and migration capacity of human EJ cells by the in situ constructed nanofiber-like nano-GP. Next, to further confirm the inhibition effect of nano-GP on CXCR4 downstream in vitro, EJ cells were incubated with saline, $Pep_{CXCR4}$, plerixafor, and bsGP (Fig. 2A). As a result, phosphorylations of extracellular signal–regulated kinase (Erk) and Akt were strongly inhibited in the bsGP-treated group (Fig. 2B). In addition, the mitogen-activated protein kinase (MAPK) pathway was suppressed in a dose-dependent manner with evidently decreased phosphorylation levels of Erk and Akt overtime in the bsGP-treated group (Fig. 2, C and D), leading to inhibition of downstream proliferation and migration cell signaling. In contrast, saline and $Pep_{CXCR4}$ did not substantially alter the phosphorylation levels of Erk and Akt. We first verified the inhibition efficiency of bsGP on the subcutaneous implantation potential of tumors in a CXCR4-dependent manner. In an EJ xenograft mice (BALB/c nude) model, the tumor tissues in the mice of each group were resected and cut into pieces for subcutaneous implantation after administration of saline, $Pep_{CXCR4}$ (500 μM, 100 μl), plerixafor (500 μM, 100 μl), or bsGP (500 μM, 100 μl) once every 2 days for a total of five times (fig. S22A). After 18 days, the tumors in saline-treated groups grew exponentially and exhibited a mean tumor volume of 1086 ± 257 $mm^3$ (fig. S22, B to D). Meanwhile, the mice in $Pep_{CXCR4}$- and plerixafor-treated groups grew exhibited a moderate tumor control with a mean tumor volume of 876 ± 118 and 647 ± 147 $mm^3$, respectively (fig. S22, B to D). In contrast, the bsGP-treated group exhibited a stronger antitumor implantation efficiency compared with saline-, $Pep_{CXCR4}$-, and plerixafor-treated groups, with an average tumor volume of 302 ± 98 $mm^3$ (fig. S22, B to D), indicating that bsGP could substantially inhibit the subcutaneous implantation potential of tumors in a CXCR4-dependent manner.

To verify the inhibitory effect of blocking CXCR4 pathway on tumor progression, we constructed a tumor model in nude mice (EJ xenograft model). The treatment methods, including the dose and frequency of administration, were consistent with the treatment conditions in the immunized mouse model (Fig. 2E). After 18 days, the tumors in saline-treated groups grew exponentially and exhibited a mean tumor volume of 2113 ± 256 $mm^3$ (Fig. 2, F to H). Meanwhile, the mice in $Pep_{CXCR4}$- and plerixafor-treated groups grew exhibited a moderate tumor control with a mean tumor volume of 1716 ± 261 and 1442 ± 133 $mm^3$, respectively (Fig. 2, F to H). Whereas, the bsGP-treated group exhibited a stronger antitumor implantation efficiency compared with saline-, $Pep_{CXCR4}$-, and plerixafor-treated groups, with an average tumor volume of 1049 ± 96 $mm^3$ (Fig. 2, F to H), indicating that bsGP could substantially inhibit the subcutaneous implantation potential of tumors in a

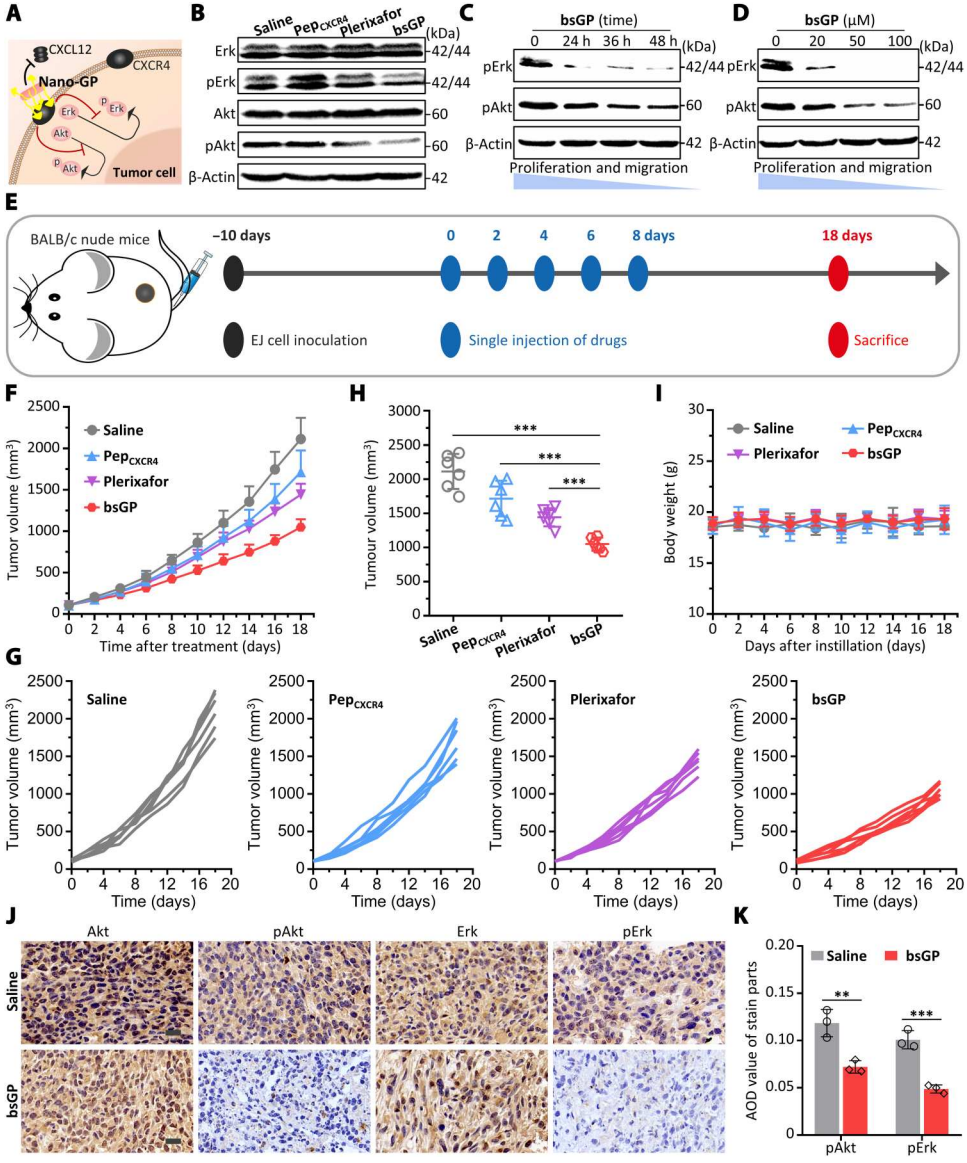


**Fig. 2. Anti-CD206/CXCR4 bsGP blocks the CXCR4 signaling pathway in vivo.** (**A**) The schematic illustration of bsGP for blocking the CXCR4 signaling pathway. (**B**) Representative Western blot analysis shows Erk, Akt, phosphorylation of Erk (pErk), and pAkt protein levels in EJ cells after treatment with saline, $Pep_{CXCR4}$ (50 μM), plerixafor (50 μM), and bsGP (50 μM) for 24 hours. (**C**) Western blot analysis shows pErk and pAkt protein levels in EJ cells after treatment with bsGP (50 μM) for 0, 24, 36, and 48 hours. (**D**) Western blot analysis shows phosphorylation of Erk and Akt protein levels in EJ cells after treatment with bsGP at 0, 20, 50, and 100 μM for 24 hours. (**E**) The schematic illustration of experimental design. (**F**) EJ xenograft tumor volumes change of each group after intravenous injection with $Pep_{CXCR4}$ (500 μM, 100 μl), plerixafor (100 μM, 100 μl), and bsGP (500 μM, 100 μl). (**G**) The individual tumor growth curves of mouse in different groups. (**H**) The average tumor volumes of EJ xenograft mice at 18 days. (**I**) Body weight changes of EJ xenograft mice in each group. (**J**) Representative images of immunohistochemistry staining of Erk, Akt, phosphorylation of Akt and Erk in tumor tissues. Scale bars, 200 μm. (**K**) Corresponding quantitative analysis results of the images of immunohistochemistry staining of phosphorylation of Erk and Aktin tumor tissues. AOD, Average optical density. $^{**}P < 0.041$ and $^{***}P < 0.001$; *P* values were determined with one-way analysis of variance (ANOVA), followed by post hoc Tukey's test. Data are presented as the means ± SD ($n = 3$).

CXCR4-dependent manner. Moreover, no obvious loss of body weight was observed after treatment with bsGP, indicating the good biosafety of bsGP (Fig. 2I). The tumor growth inhibition rate was 50% for bsGP group, while it was 19% for the $Pep_{CXCR4}$ group and 32% for the plerixafor group. Moreover, we further confirmed the inhibition of CXCR4 downstream in vivo. As a result, the phosphorylation levels of Erk and Akt were strongly inhibited in bsGP-treated tumor tissues compared with that in saline-treated tumor tissues (Fig. 2, J and K), suggesting that bsGP could arrest CXCR4 signaling in vivo. Together, these results strongly demonstrated that the nanofiber-like nano-GP constructed on the surface of tumor cells substantially enhanced the inhibition of CXCR4 signaling, thus inhibiting the proliferation and migration capacity of tumors.

### Anti-CD206/CXCR4 bsGP targets tumor cell and TAMs to inhibit tumor progression

Subsequently, we validated the spatial synergistic effect of two targeting modules of bsGP in the inhibitory of tumor progression. When the tumor volume of MB49-Luc bladder cancer mice (C57BL/6) was approximately 100 $mm^3$, the mice were administrated with saline, prepared nano-GP (CXCR4-targeting peptide with self-assembly motif), tri-Man (tri-mannose alone), prepared nano-GP + tri-Man (the mix of these two as a combination therapy), bsGP-uC, or bsGP once every other day for a total of five times (Fig. 3A). After treatment for 18 days, the tumors in the saline-treated groups grew exponentially and exhibited a mean tumor volume of 1860 ± 180 $mm^3$ (Fig. 3, B and C). Meanwhile, the mice in the prepared nano-GP–, tri-Man–, prepared nano-GP + tri-Man–, bsGP-uC–treated groups grew exhibited a moderate tumor control with an average tumor volumes of 1483 ± 138, 1582 ± 194, 1064 ± 239, and 1171 ± 253 $mm^3$, respectively (Fig. 3, B and C). Whereas, the bsGP-treated group exhibited a stronger antitumor efficiency with a mean tumor volume of 591 ± 197 $mm^3$ (Fig. 3, B and C), indicating that MMP-2–tailored bsGP could substantially inhibit the progression of tumors than that of MMP-2–untailored bsGP. At the end of treatment protocol, all mice were euthanized to collect tumor tissues (Fig. 3, E and F), which suggests that tumor growth inhibition rate was 75% for bsGP group, while it was 11% for the prepared nano-GP group, 8% for the tri-Man group, 26% for the prepared nano-GP + tri-Man group, and 23% for the bsGP-uC group. We hypothesized that the CXCR4 signaling pathway could not be effectively inhibited because of the fact that bsGP-uCs were more easily phagocytic by TAMs. Moreover, no obvious loss of body weight was observed after treatment with bsGP, indicating the good biosafety of bsGP (Fig. 3D). Together, these results strongly demonstrated that the importance of the spatial synergistic effect of two targeting modules of bsGP and the nanofiber-like nano-GP constructed on the surface of tumor cells substantially enhanced the inhibition of CXCR4 signaling.

### Anti-CD206/CXCR4 bsGP recruits and redirects T lymphocytes in tumor tissues

Subsequently, orthotopic bladder cancer mice (BALB/c) were built to further evaluate the specific targeting and persistence of bsGP in tumors through intravesical instillation (Fig. 4A). Fluorescence images of in vivo and ex vivo tumor-bearing bladders were obtained after intravesical instillation of bsGP (500 μM, 100 μl) (fig. S23). Moreover, evident fluorescence signals were observed at the tumor site in both the $Pep_{CXCR4}$ and bsGP groups, indicating the high specificity of bsGP toward bladder cancer by intravesical instillation (Fig. 4B). To further verify that bsGP could regulate the repolarization of macrophages at molecular level, the expression of major proteins in macrophages (RAW264.7) cultured with saline, mannose, and bsGP was evaluated with Western blotting. The results showed that bsGP effectively activated the phosphorylation of nuclear factor κB (NF-κB) compared with mannose (Fig. 4C). Meanwhile, the phosphorylation of NF-κB in tumor tissues was evaluated with Western blotting after treatment with saline, mannose, and bsGP once every 2 days for a total of five times. The results showed that bsGP effectively activated the phosphorylation of NF-κB compared with mannose (fig. S24). Subsequently, orthotopic bladder cancer mice were used to validate the polarization of TAMs in vivo based on bsGP (Fig. 4D). Tumor tissues were harvested and analyzed with flow cytometry 10 days after treatment with saline, $Pep_{CXCR4}$ (500 μM, 100 μl), and bsGP (500 μM, 100 μl). As shown in Fig. 4E, the proportion of M2-type macrophages was substantially decreased by approximately 11.9% (from 29.2 to 17.3%), together with an increased polarization of M1-like TAMs by approximately 11.2% (from 14.2 to 25.4%) after treatment with bsGP (fig. S25). These results suggested that bsGP could efficiently induce the polarization of TAMs to the M1 phenotype, which could modulate the tumor immune microenvironment. In addition, the intratumoral concentrations of cytokines, including interleukin-10 (IL-10), IL-12, tumor necrosis factor–α (TNF-α), and transforming growth factor–β (TGF-β), were detected in the homogenized tumor tissues. Compared with the saline and $Pep_{CXCR4}$ groups, the bsGP treatment group substantially up-regulated the intratumoral secretion of TNF-α and IL-12 and, meanwhile, down-regulated the secretion of IL-10 and TGF-β, further demonstrating the effective immune responses induced by bsGP (fig. S26). Meanwhile, the proportion of $CD45^+CD3^+CD8^+$ T cells in the bsGP-treated tumor tissue was substantially higher than that from mice treated with saline (25.8% versus 16.3%) (figs. S27 and S28). Moreover, the relative abundance of granzyme $B^+CD8^+$ T cells at the tumor site was substantially higher in mice that received bsGP treatment than that in mice treated with saline (19.60% versus 9.44%) (figs. S27 and S28). Besides, the relative abundance of $CD4^+Foxp3^+$ $T_{regs}$ at the tumor site was substantially lower in mice that received bsGP treatment than that in mice treated with saline (6.80% versus 8.58%) (figs. S27 and S28). The results indicated that bsGP increased the number and activity of $CD8^+$T cells in tumor.

How tumor cells and TAM interactions were regulated and how they were spatially organized within tumors after treatment with bsGP. MB49-Luc tumor-bearing mice (C57BL/6) were treated with saline, $Pep_{CXCR4}$ (500 μM, 100 μl), and bsGP (500 μM, 100 μl) once every other day for five times. Multiplex immunofluorescence approaches have been shown to more accurately explore cellular functional states and spatial and functional interactions between multiple cell types, as well as how these interactions were modulated by bsGP.

Most notably, bsGP exhibited the strongest ability to increase the number of $CD86^+$ M1-like TAMs by 2.3-fold (19.19%) (Fig. 4, F and G, and fig. S29A) and decrease the number of $CD206^+$ M2-like TAMs from 20.94 to 13.0% (Fig. 4, F and G, and fig. S29A) in tumor tissues. These data comprehensively and visually presented that bsGP efficiently repolarizes M2-like TAMs to the M1 phenotype. $CD8^+$ T cells are recruited by M1-like TAMs by secreting some chemokines and cytokines, such as CXCL-9, CXCL-10, CXCL-11, and TNF-α (*39*). Immunofluorescence analysis showed that the frequencies of tumor-infiltrating $CD8^+$ T cells (9.07%) in the bsGP group were increased 2.6-fold compared with that in the saline group (3.43%) and the $Pep_{CXCR4}$ group (4.04%) (Fig. 4, H and I, and fig. S29B). At the same time, the $CD4^+$ T cells (4.35%) in the bsGP group were also increased 2.5-fold compared with that in the saline group (1.74%) and the $Pep_{CXCR4}$ group (2.37%) (Fig. 4, H and I, and fig. S29B). This suggested that infiltrating T cell specifically in the bsGP group could be important in the antitumoral immune response.

The close interaction of immune cells with tumor cells was demonstrated to predict the response to cancer immunotherapy, highlighting the importance of also taking the spatial interactions of

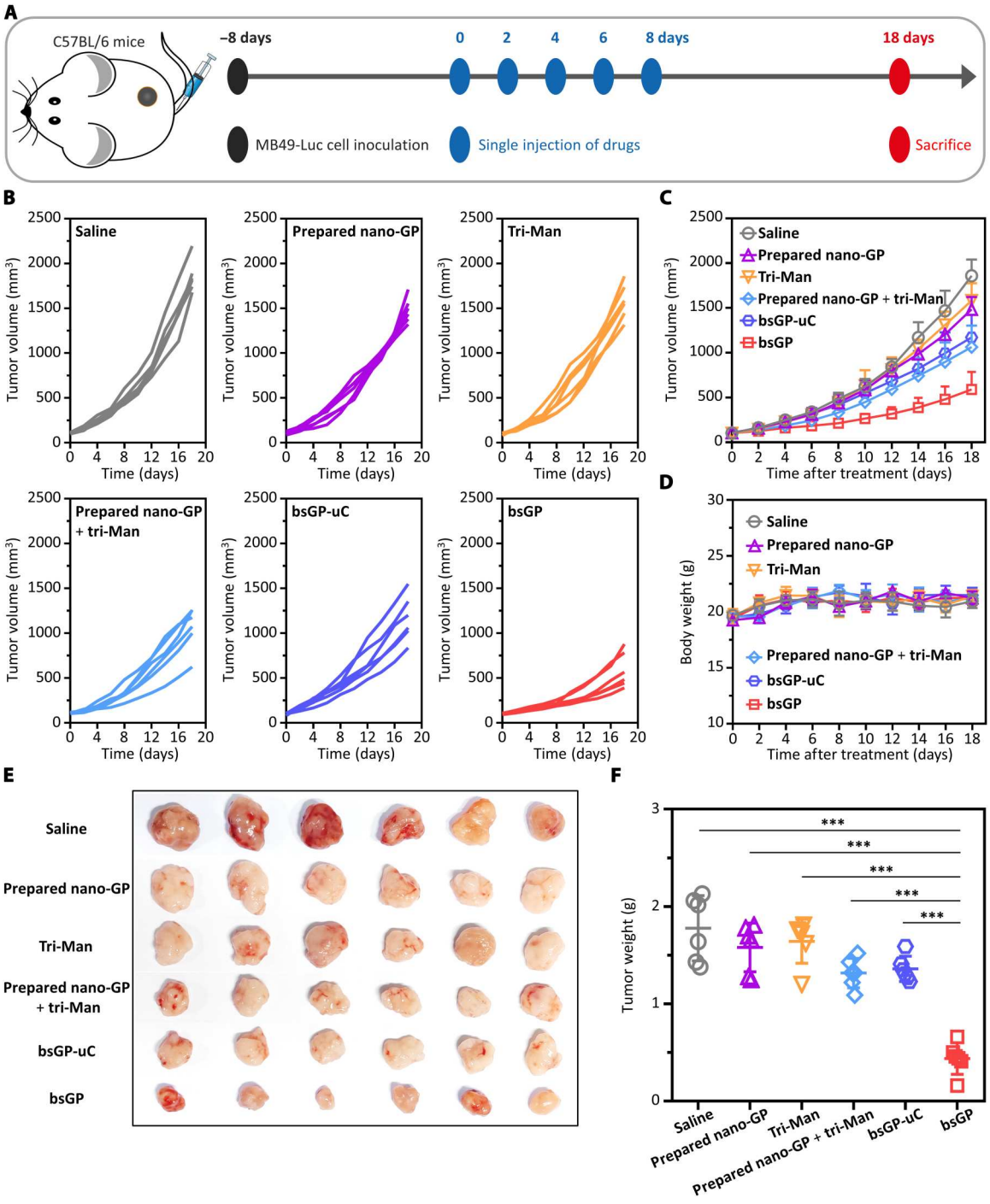


**Fig. 3. Anti-CD206/CXCR4 bsGP inhibit the tumor progression in vivo.** (**A**) The schematic illustration of bsGP for experimental design. (**B**) The individual tumor growth curves of mouse in the saline, prepared nano-GP (CXCR4-targeting peptide with self-assembly motif; 500 μM, 100 μl), tri-Man (tri-mannose alone; 500 μM, 100 μl), bsGP-uC (bsGPs with MMP-2 uncleavable linker; 500 μM, 100 μl), prepared nano-GP (500 μM, 100 μl) + tri-Man (500 μM, 100 μl) (the mix of these two as a combination therapy), or bsGP (500 μM, 100 μl) groups. (**C**) Time-dependent MB49-Luc tumor volumes change of each group. (**D**) Body weight changes of MB49-Luc bladder cancer mice in each group. (**E** and **F**) The tumor image and weights of MB49-Luc bladder cancer mice at 18 days after incubation. ***$P < 0.001$; $P$ values were determined with one-way ANOVA, followed by post hoc Tukey's test. Data are presented as the means ± SD ($n = 6$).

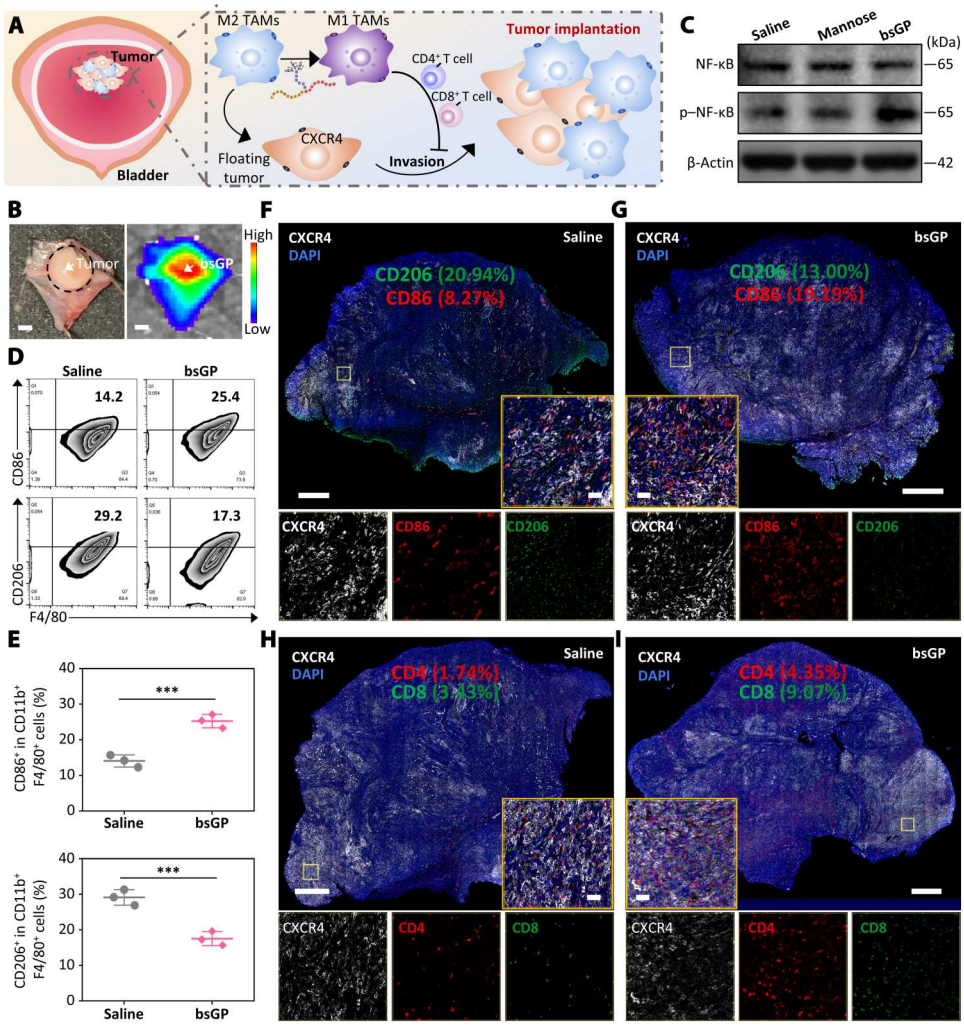


**Fig. 4. Anti-CD206/CXCR4 bsGP recruits of T lymphocytes in vivo.** (**A**) Schematic illustration of the recognition specificity and immune response induced by bsGP. (**B**) Representative bright field and corresponding ex vivo fluorescence image of the tumor-bearing bladder. Scale bars, 2 mm. (**C**) Representative Western blot analysis shows NF-κB and p–NF-κB protein levels in RAW264.7 cells after treatment with saline, mannose (50 μM), and bsGP (50 μM) for 24 hours. (**D**) Representative flow cytometry analysis images and (**E**) the relative quantification of M2-like macrophages (CD206) and M1-like macrophages (CD86) gating on F4/80$^+$ CD11b$^+$ cells. Representative immunofluorescence images illustrating the proportion of CD86$^+$ M1-like TAMs and CD206$^+$ M2-like TAMs in the whole tumor slice after treatment with saline (**F**) or bsGP (500 μM, 100 μl) (**G**) by intravesical instillation every other day for five times. The cell nucleus was stained with 4′,6-diamidino-2-phenylindole (DAPI). CXCR4 is in white, CD86 is in red, and CD206 is in green. Scale bars, 1 mm. Representative immunofluorescence images illustrating the proportion of CD4$^+$ T cells and CD8$^+$ T cells in the whole tumor slice after treatment with saline (**H**) or bsGP (500 μM, 100 μl) (**I**) by intravesical instillation every other day for five times. The cell nucleus was stained with DAPI. CXCR4 is in white, CD4 is in red, and CD8 is in green. Scale bars, 1 mm. ***$P < 0.001$; $P$ values were determined with one-way ANOVA, followed by post hoc Tukey's test. Data are presented as the means ± SD ($n = 3$).

immune cells within the TME into account (*39*). To further validate this spatial association at single-cell resolution, we performed whole-section staining to provide a more comprehensive map of the spatial interactions between multiple cell types (such as tumor cells, TAMs, and T cells) modulated by bsGP. Notably, with tumor cells as the center, the number of CD86$^+$ M1-like TAMs in the bsGP group was up to $6.22 \times 10^4$ in the 5- to 10-μm radius and increased 2.6 times compared to the saline group (Fig. 5, A to C). The number of CD206$^+$ M2-like TAMs in the bsGP group was decreased by 20% compared to that in the saline group in the 5- to 10-μm radius (Fig. 5, A, B, and D). Although the number of macrophages was relatively small at a distance from the tumor cells, the regulation of macrophages by bsGP was highly efficient within a 100-μm radius (Fig. 5, C and D, and fig. S30). We hypothesized that T cells would be spatially organized close around cells expressing T cells attracting chemokines (*39*). Across all samples, CD8$^+$ T cells and CD4$^+$ T cells in the bsGP group were, on average, closer to CXCR4$^+$ tumor cells than the saline and $Pep_{CXCR4}$ counterparts, and these distances were especially small within foci (CXCR4$^+$ tumor cells) (*39*). In the bsGP group, the numbers of CD8$^+$ T cells and CD4$^+$ T cell infiltration at a 10-μm distance from foci were increased 5.5-fold and 4.0-fold compared to that in the saline group, respectively (Fig. 5, E to H, and fig. S31). Moreover, we further investigated whether the inhibition of CXCR4 downstream in vivo could facilitate T cell infiltration through decreases tumor fibrosis. As a result, the tumor fibrosis was strongly inhibited in bsGP-treated tumor tissues compared

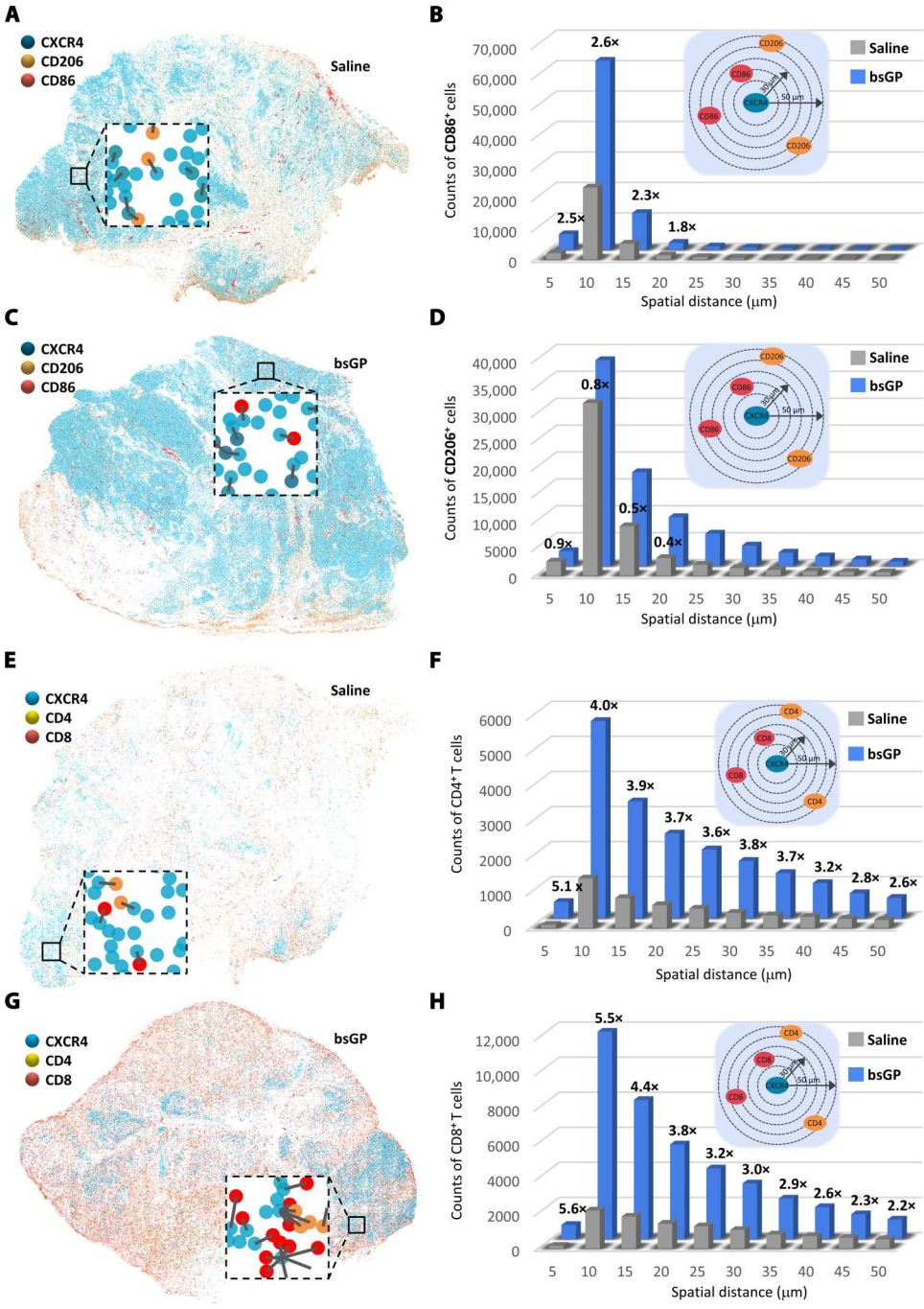


**Fig. 5. Anti-CD206/CXCR4 bsGP redirects T lymphocytes to tumor cell in vivo.** (**A** and **C**) Representative images illustrating CD86$^+$ M1-like TAMs and CD206$^+$ M2-like TAMs in proximity to CXCR4$^+$ tumor cells after treatment with saline and bsGP (500 μM, 100 μl) by intravesical instillation every other day for five times. (**B**) Counts of CD86$^+$ M1-like TAMs proximal to the tumor within 50 μm in spatial distance. (**D**) Counts of CD206$^+$ M2-like TAMs proximity to tumors within 50 μm in spatial distance. (**E** and **G**) Representative images illustrating CD4$^+$ T cell and CD8$^+$ T cell proximity to CXCR4$^+$ tumor cells after treatment with saline and bsGP (500 μM, 100 μl) by intravesical instillation every other day for five times. (**F**) Counts of CD4$^+$ T cells proximal to the tumor within 50 μm in spatial distance. (**H**) Counts of CD8$^+$ T cells proximity to tumors within 50 μm in spatial distance.

with that in saline- and $Pep_{CXCR4}$-treated tumor tissues (fig. S32), suggesting that bsGP could decrease tumor fibrosis in vivo. We speculated that high $CD8^+$ T cell and $CD4^+$ T cell infiltration was substantially associated with high frequencies of $CD86^+$ M1-like TAMs, which may be critical for the formation of these immune cell hotspots within tumors. On the other hand, CXCR4 signaling was blocked, which reduced tumor fibrosis and promoted T cell infiltration. Our findings thus reveal that bsGP modulates spatially organized foci of $CD8^+$ T cells and $CD4^+$ T cells, $CD86^+$ M1-like TAMs, and tumor cells, providing a platform for frequent encounters of T cells with other cells to coordinate immune responses.

### Anti-CD206/CXCR4 bsGP inhibits tumor recurrence

Ultimately, the therapeutic effects of bsGP on tumor implantation recurrence were further investigated in an orthotopic bladder cancer mice (C57BL/6) model. Tumor tissue homogenates were intravesically instilled into the damaged bladder cavity to simulate the postoperative conditions of bladder cancer. Afterward, saline, plerixafor (CXCR4 antagonist, 0.05 mg/ml, 100 μl), doxycycline (Dox; first-line clinical drug, 1 mg/ml, 100 μl), BCG (first-line clinical drug, 1 mg/ml, 100 μl), and bsGP (2 mg/ml, 100 μl) were intravesically instilled into the bladder for treatment (Fig. 6A). The progress of tumor implantation was further monitored by bioluminescence signals from MB49-Luc tumor cells (Fig. 6, A and B). Compared with the substantially decreased survival rate in the saline (0%), plerixafor (0%), Dox (11%), and BCG (22%) groups at 60 days after treatment, 78% of the mice survived for at least 60 days after bsGP treatment (Fig. 6C). bsGP substantially reduced the postoperative recurrence of bladder cancer in orthotopic tumor-bearing mice, with a recurrence rate of only 22%, while 100% recurred in the saline and plerixafor groups, and the recurrence rates were up to 89 and 78% in the Dox and BCG groups, respectively (Fig. 6, D and E), indicating that bsGP generates superior therapeutic effects for the inhibition of tumor recurrence at the therapeutic dose that we used (2 mg/ml, five times) in the orthotopic bladder cancer mice model.

Furthermore, we investigated the systemic toxicity of bsGP treatment. Mice (C57BL/6) were treated with bsGP without loss of body weight (fig. S33). Notably, no signs of a deteriorating general condition, such as red skin or reduced food consumption, were observed. Moreover, to evaluate the on-target off-tumor side effects of bsGP treatment, histological analysis of major organs was harvested from mice at 1 day after treatment. Urinalysis together with the serum biochemistry assay was conducted at 1, 7, and 14 days after treatment with saline and bsGP by intravesical instillation. As a result, the main organs had no obvious tissue damage in hematoxylin and eosin (H&E) staining (fig. S34A). Meanwhile, no inflammation or hematuresis was observed in the results of urinalysis laboratory report analyses (fig. S34B). No noticeable difference was observed between the saline and bsGP-treated groups regarding the levels of major liver and kidney function markers (fig. S34, C to F). Above results demonstrated that bsGP treatment did not induce severe systemic toxicity in vivo, indicating that bsGP has good biosafety at the treatment dose, which was highly encouraging for applications in clinical research.

## DISCUSSION

Tumor progression is dependent not only on the characteristics of malignant cells but also on the behavior of the whole TME. Dual-targeting concepts enabled by bispecific antibody, which provide simultaneous targeting of more cancer-mediating receptors or crosstalk signaling cascades, are thought to increase the chance of effectively addressing receptor redundancy or heterogeneity. We developed a bsGP (CD206 × CXCR4) based on the physiological characteristics of the TME in early postoperative tumor cell implantation. We exploited innovative therapeutic concepts (CD206 × CXCR4) and unlocked functionalities of precise temporal and spatial control of the targets of the CD206 and CXCR4 receptor. The results indicated that bsGP promoted the repolarization of M2-like TAMs to the M1-like phenotype close to surrounding tumor cells and simultaneously long-term arrest of CXCR4 signaling could be modulated spatially organized foci of $CD8^+$ T cells and $CD4^+$ T cells, $CD86^+$ M1-like macrophages, and malignant cells, resulting in remodeling of the tumor immunosuppressive TME. Our results highlighted the importance of taking the spatial interactions of multiple cell types (such as tumor cells, TAMs, and T cells) within the TME into account on tumor therapy. However, in the design of bispecific functional molecules, the combination of bifunctional targets is also very important, which determines the cascade of functions. bsGP substantially reduced the postoperative recurrence of bladder cancer in orthotopic tumor-bearing mice, with a recurrence rate of only 22%, while all recurred in the saline and plerixafor groups, and the recurrence rate up to 89 and 78% in Dox and BCG groups, respectively. This developed bsGP (CD206 × CXCR4) demonstrated great advantages over multicellular temporal and spatial organization, which will provide a promising therapeutic strategy for the inhibition of tumor recurrence with diverse biomedical applications.

## MATERIALS AND METHODS

### Materials

All amino acids and Wang resin were purchased from Gill Biochemical (Shanghai, China). L929, EJ, and MB49-Luc cell lines were derived from the Cell Culture Center of the Institute of Basic Medicine, Chinese Academy of Medical Sciences (Beijing, China). The BCA Protein Assay Kit (B5000) and RIPA Lysis Buffer (R1091) were purchased from LABLEAD Inc. (Beijing, China). Sterile PBS (SP02010500) and 10× Tris Buffered Saline with Tween 20 (TBST) were purchased from Sperikon Life Science & Biotechnology Co. Ltd. Matrigel (M8370), D-luciferin sodium salt (IL0230), and 4′,6-diamidino-2-phenylindole (DAPI) (D8200) were purchased from Beijing Solarbio Science & Technology Co. Ltd. (Beijing, China). Anti-CXCR4 rabbit mAb (ab124824) was purchased from Abcam Trading Co. Ltd. (Shanghai, China). Akt (pan) (C67E7) rabbit mAb, phospho-Akt ($Thr^{308}$) (D25E6) XP rabbit mAb, p44/42 MAPK (Erk1/2) (137F5) rabbit mAb, phospho-p44/42 MAPK (Erk1/2) ($Thr^{202}$/$Tyr^{204}$) (D13.14.4E) XP rabbit mAb, and β-actin (8H10D10) mouse mAb were purchased from Cell Signaling Technology Inc. PerCP/Cyanine5.5 anti-mouse CD86, phycoerythrin (PE) anti-mouse CD206, allophycocyanin (APC) anti-mouse F4/80, fluorescein isothiocyanate (FITC) anti-mouse/human CD11b, Alexa Fluor 700 anti-mouse CD45, BV421 rat anti-mouse CD25, Brilliant Violet 605 anti-

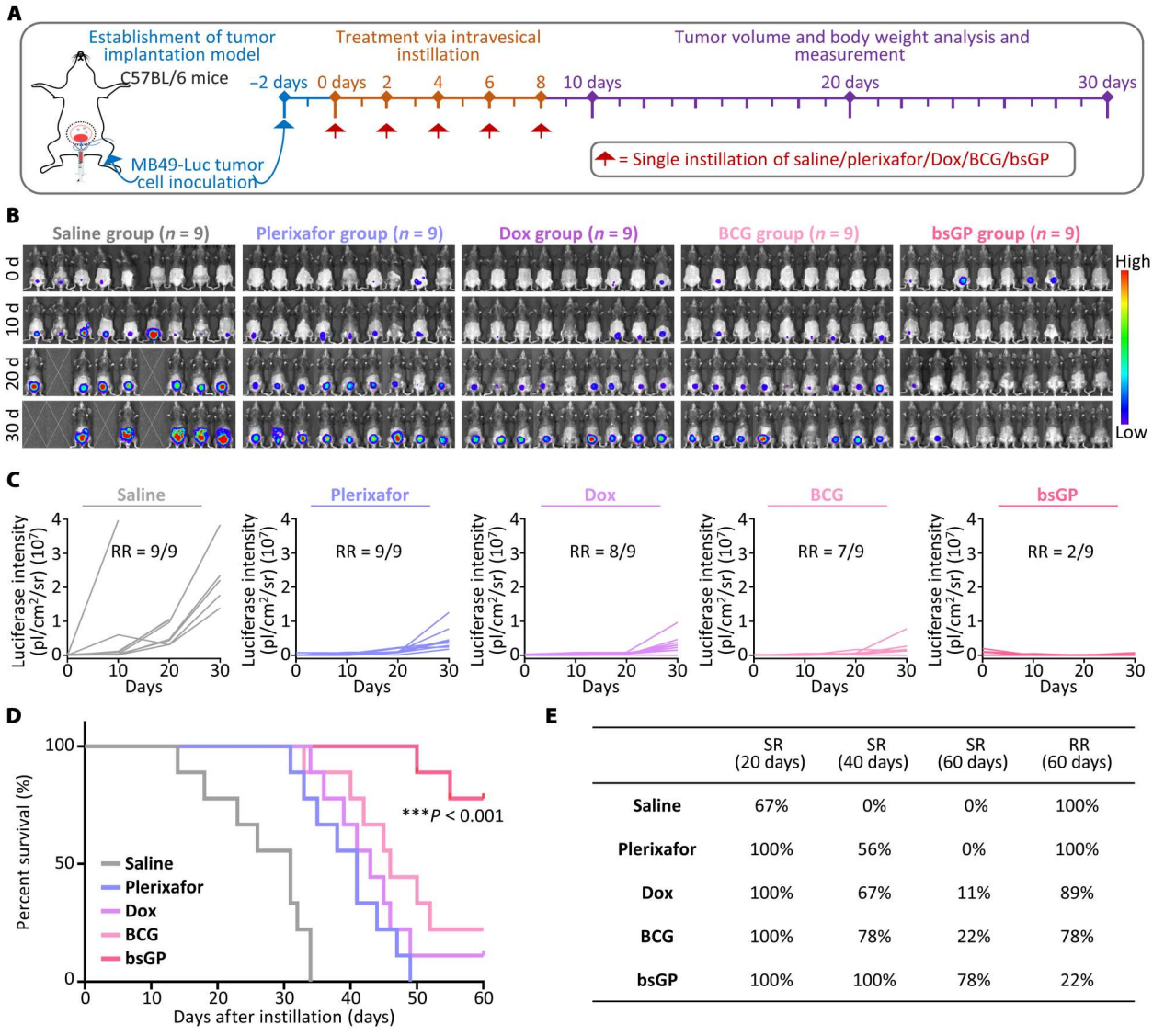


| | SR (20 days) | SR (40 days) | SR (60 days) | RR (60 days) |
|---|---|---|---|---|
| **Saline** | 67% | 0% | 0% | 100% |
| **Plerixafor** | 100% | 56% | 0% | 100% |
| **Dox** | 100% | 67% | 11% | 89% |
| **BCG** | 100% | 78% | 22% | 78% |
| **bsGP** | 100% | 100% | 78% | 22% |

**Fig. 6. The inhibitory effect of anti-CD206/CXCR4 bsGP on tumor recurrence.** (**A**) Schematic illustration of the experimental design. Saline, plerixafor (0.05 mg/ml, 100 μl), Dox (1 mg/ml, 100 μl), BCG (1 mg/ml, 100 μl), and bsGP (2 mg/ml, 100 μl) were intravesically instilled into the bladder twice every other day for five times. (**B**) In vivo bioluminescence images of orthotopic bladder cancer mice after treatment with saline, plerixafor, Dox, BCG, and bsGP at 0, 10, 20, and 30 days after instillation. (**C**) Quantitative bioluminescence intensity at the bladder site of orthotopic bladder cancer mice in each group. (**D**) The Kaplan-Meier survival curve of orthotopic bladder cancer mice in each group. (**E**) The survival rate (SR) and recurrence rate (RR) of orthotopic bladder cancer mice at 20, 40, and 60 days after instillation. ***$P < 0.001$; $P$ values were determined with one-way ANOVA, followed by post hoc Tukey's test. Data are presented as the means ± SD ($n = 9$).

mouse CD3ε, PE/Cyanine7 anti-mouse CD8a, Alexa Fluor 647 anti-mouse Forkhead box protein P3 (FOXP3), and FITC anti-human/mouse granzyme B recombinant were purchased from BioLegend (Beijing) Ltd. Recombinant CXCR4 (RPA940Hu01) was purchased from CLOUD-CLONE CORP. The mouse IL-10 enzyme-linked immunosorbent assay (ELISA) kit (CZM04-96), mouse IL-12 ELISA kit (CZM16-96), mouse TGF-β ELISA kit (CZM03-96), and mouse TNF-α ELISA kit (CZM02-96) were purchased from Beijing Chengzhi Kewei Biotechnology Co. Ltd. Female BALB/c nude mice and female C57BL/6 mice were purchased from Vital River Laboratory Animal Technology Co. Ltd. (Beijing, China).

## Synthesis and characterization of bsGP

bsGP [LGASWHRPDKK(PLGYLG-$(man)_3$)LVFFAECG] was synthesized according to solid-phase peptide synthesis (SPPS) and characterized with electrospray ionization mass spectrometry (ESI-MS) and HPLC. The detailed synthesis procedures were shown as below: GP1 [LGASWHRPDKK(PLGYLG-$(Ac\text{-}man)_3$-)LVFFAECG] was synthesized according to the 9-fluorenyl methoxycarbonyl (Fmoc) approach of SPPS. First, the main chain sequence of the peptide (LGASWHRPDKKLVFFAECG) was synthesized on resin with the Boc-Leu-OH and Fmoc-Lys (Dde)-OH underlined and then continued to synthesize the branch chain sequence [PLGYLG-$(Ac\text{-}man)_3$] in the amino group of the side chain K [Fmoc-Lys (Dde)-OH] and 5-acetynoic acid coupling in the last

amino Pro. Last, Ac–tri-Man was coupled by standard copper(I)-catalyzed azide-alkyne cycloaddition (CuAAC) conditions in the presence of substoichiometric amount of CuBr and Tris(benzyltriazolylmethyl)amine (TBTA) in *N*,*N*′-dimethylformamide–afforded GP1 after cleavage of the peptide from the resin. The final product bsGP {LGASWHRPDKK[PLGYLG-$(man)_3$]LVFFAECG} was obtained by removing the acetyl group in methanol/$H_2O$ mixture (0.1 M NaOH). bsGP-uC {LGASWHRPDKK[PGSGSG-$(man)_3$]LVFFAECG}, $Pep_{CXCR4}$ (LGASWHRPDK), and nano-GP [LGASWHRPDKK(YLG)LVFFAECG] were synthesized according to SPPS and characterized with ESI-MS and HPLC.

### Immunohistochemistry of CXCR4 in human bladder cancer

Immunohistochemistry of CXCR4 in human bladder cancer tissues was performed by Wuhan Servicebio Technology Co. Ltd. All the experiments using human specimens were reviewed and approved by the Committees for Ethical Review of the Fourth Hospital of Harbin Medical University (2022-SCILLSC-33) after obtaining appropriate informed consent.

### CD spectra

The secondary structures of bsGP and nano-GP were monitored by CD spectroscopy (JASCO Corporation, JC-1500) with a cell path length of 1 cm at room temperature. bsGP (10 μM) and nano-GP (10 μM) were dissolved in deionized water at 25°C for 1 hour. Then, the measurements were carried out under a scanning speed of 500 nm/min and a resolution of 0.5 nm. The solution background was carefully subtracted to correct the spectra obtained.

### FTIR spectra

The molecular arrangement and secondary structures of bsGP and nano-GP were further analyzed by FTIR. The bsGP and nano-GP at concentrations of 100 μM were freshly prepared in distilled water for 60 min. Then, sample solutions were dropped on calcium fluoride tablets and dried. Last, the FTIR spectra of bsGP and nano-GP were recorded on a MAGNA-IR 560.

### In vitro recombinant protease assays

bsGPs (25 μg) was incubated with recombinant human MMP-2 (Abcam, ab81550) in a final volume of 50 μl in enzyme-specific buffers [50 mM tris, 150 mM NaCl, 5 mM $CaCl_2$, and 1 μM $ZnCl_2$ (pH 7.5)] at 37°C for 120 min. The final MMP-2 concentration was 5 μg/ml.

### TEM and AFM

The morphologies of nano-GP were characterized by TEM on a Tecnai G2 20 S-TWIN electron microscope. The nano-GP (50 μM, 50 μl) samples were dropped on copper meshes at room temperature for 10 min. Then, excessive liquid was removed, followed by staining with 2% uranyl acetate for 40 s. Last, the copper meshes were dried at room temperature for observation. The nano-GP (50 μM, 50 μl) samples were drop-casted on a freshly cleaved mica surface for 20 min. Then, the excessive solutions were withdrawn from the mica surface, followed by nitrogen gas drying before AFM observations. AFM experiments were performed on Bruker MultiMode 8.

### Microscale thermophoresis ligand binding measurements

To test the affinity of nano-GP with CXCR4, bsGP with CD206, microscale thermophoresis (MST) assay was conducted by using Monolish NT.115 (NanoTemper Technologies). CXCR4 and CD206 were labeled using the Protein Labeling Kit RED-NHS (NanoTemper Technologies). The labeling reaction was performed according to the manufacturer′s instructions in the supplied labeling buffer applying a concentration of 20 μM protein (molar dye: protein ratio ≈ 3:1) at room temperature for 30 min in the dark. Unreacted dye was removed with the supplied dye removal column equilibrated with MST buffer [50 mM tris-HCl (pH 7.8), 150 mM NaCl, and 10 mM $MgCl_2$]. We first prepared nano-GP solutions of 400 μM in saline with 2% dimethylsulfoxide for 24 hours of incubation and ultrasonic blending and then diluted them into saline to reach concentration gradients. We made sure that nano-GP was about the diameter of 23.6 ± 2.1–nm nanoparticle at each concentration tested. The measured affinity is the apparent $K_d$ of a nanoparticle to CXCR4 protein. For each assay, the labeled protein (400 nM) was incubated with series of bsGP or nano-GP concentration gradients. The samples were loaded into the silica capillaries (Monolith NT.115 Standard Treated Capillaries, MO-K002; Monolith NT.115 MST Premium Coated Capillaries, MOK005) and measured using Monolish NT.115 (NanoTemper Technologies) at medium MST power, 5% or 20% light-emitting diode power. The data were further analyzed by MO.Affinity Analysis software.

### Cell viability assays

The cytotoxicity of bsGP and $Pep_{CXCR4}$ was evaluated using a CCK-8 assay with EJ and RAW264.7 cells. Cells at a density of $5 \times 10^4$ per well were seeded into 96-well plates in RPMI 1640 medium, followed by culture at 37°C in a humidified atmosphere with 5% $CO_2$ overnight. Then, bsGP and $Pep_{CXCR4}$ sample solutions (10 μl) at different concentrations (10, 20, 50, 100, 200, and 500 μM) were added to each well, and the cells were incubated for another 24 hours. Subsequently, CCK-8 solutions were added to each well, followed by incubation for another 2 hours at 37°C. Last, the cell viability was analyzed by measuring the absorbance values of the cells per well at 450 nm for the test wavelength and 690 nm for the reference wavelength by a microplate reader. Saline groups were conducted under the same condition. The cell viability rate was calculated with the following equation

$$\text{The cell viability} = (A_s - A_b)/(A_c - A_b) \times 100\%,$$

where $A_s$ represents the absorbance of cells in the bsGP- and $Pep_{CXCR4}$-treated groups, $A_c$ represents the absorbance of cells in the saline-treated groups, and $A_b$ represents the absorbance of blank groups. All experiments were performed in triplicate.

### Western blot

EJ cells treated under different conditions were collected by centrifugation for 15 min after lysis with lysis buffer containing protease inhibitor. Total cellular proteins were measured using a BCA kit. Samples (30 μg of protein) were subjected to SDS–polyacrylamide gel electrophoresis (PAGE) and transferred to polyvinylidene difluoride (PVDF) membranes. After blocking for 1 to 2 hours at room temperature with blocking buffer containing 5% (w/v) nonfat milk and 0.1% (v/v) Tween 20 in 10 mM tris-buffered saline, the PVDF membranes were incubated with primary

antibodies overnight at 4°C. Then, the membranes were washed (four times for 7 min) with TBST and incubated with an appropriate secondary antibody for 1 to 2 hours at room temperature. Last, signals were observed by chemiluminescence on a Typhoon Trio variable mode imager.

### Flow cytometry analysis

MB49-Luc tumor tissues from mice treated under different conditions were collected and digested in RPMI 1640 medium containing with collagenase I (1 mg/ml) to form single-cell suspensions. After filtered with a 70-μm cell strainer, the supernatant from the digested tumor tissues was washed three times with PBS and centrifugated. The resultant single-cell suspensions were stained with fluorescence antibodies [PerCP/Cyanine5.5 anti-mouse CD86, PE anti-mouse CD206, APC anti-mouse F4/80 and FITC anti-mouse/human CD11b for macrophages, Alexa Fluor 700 anti-mouse CD45; BV421 rat anti-mouse CD25, Brilliant Violet 605 anti-mouse CD3ε, PE/cyanine7 anti-mouse CD8a, Alexa Fluor 647 anti-mouse FOXP3, and FITC anti-human/mouse granzyme B recombinant for T cells] for 30 min according to the manufacturer′s instructions. Last, the stained cells were studied with a CytoFLEX flow cytometer (Beckman) and FlowJo software to analyze the macrophages.

### Cellular imaging experiment

EJ cells at a density of $1 \times 10^4$ were cultured in a confocal microscope dish (1 ml) at 37°C in a humified atmosphere containing 5% $CO_2$ for 24 hours. Then, the cells were incubated with bsGP (50 μM, pH 7.4, saline) at 37°C for 15 min, followed by washing with saline three times. Last, the cells were imaged with CLSM (UltraVIEW VoX) in a 40× objective lens.

### Morphology observation by SEM

A density of $1 \times 10^5$ EJ cells per well were seeded onto silicon wafers in 12-well plates and cultured for 12 hours. Then, saline, $Pep_{CXCR4}$ (50 μM), and bsGP (50 μM) were added to each well and incubated for an additional 12 and 24 hours, respectively. Then, the cells were solidified with glutaraldehyde (4%) and dehydrated with a graded series of alcohols (50, 70, 80, 90, and 100), followed by coating with gold for 90 s. Last, the specimens were observed with a Nova Nano 430 SEM (FEI).

### Zymography

The activity of MMP-2 in L929 and EJ cells was assessed with a zymography assay kit. Briefly, the cell culture supernatants were collected and centrifuged at 2000 rpm for 10 min at 4°C after culture in serum-free medium for 24 hours. Subsequently, 20 μl of the supernatant was subjected to SDS-PAGE at 4°C. After electrophoresis, the gel was eluted with buffer A every 15 min for a total of four times and further incubated with buffer B for 48 hours at 37°C. Last, the gels were stained with SimplyBlue and scanned with a Typhoon Trio variable mode imager for analysis.

### Colony formation assay

Different groups of EJ cells at a density of 200 in Dulbecco′s modified Eagle medium (DMEM) were cultured in six-well plates at 37°C in a humified atmosphere containing 5% $CO_2$ for 24 hours. When visible colonies appeared in the six-well plates, the supernatant was discarded and carefully rinsed twice with saline. Then, the colonies were fixed with 4% paraformaldehyde for 15 min. Last, the fixed cells were stained with Giemsa stain solution for 10 to 30 min, followed by photographing with a microscope for counting and analysis.

$$\text{Colony formation efficiency} = (\text{number of clones}/\text{numbers of inoculated cells}) \times 100\%.$$

### Transwell assay

EJ cells at a density of $1 \times 10^5$ in 150 μl of serum-free DMEM were seeded in apical chamber of Transwell chambers and treated with saline, $Pep_{CXCR4}$ (50 μM), or bsGP (50 μM). Subsequently, complete medium was added to the basolateral chamber. Next, the EJ cells in the apical chambers were removed using a cotton swab after 24 hours, and the migrated EJ cells were fixed with 4% paraformaldehyde. Last, the fixed cells were stained with 0.05% crystal violet for 10 min, followed by photographing with a microscope for counting and analysis.

### Establishment of orthotopic bladder cancer xenograft model

All animal experiments complied with the *Guide for the Care and Use of Laboratory Animals* and were approved by the Committee for Animal Research of National Center for Nanoscience and Technology (NCNST21-2202-0606). Female BALB/c nude mice (6 to 8 weeks, 16 to 18 g) were anesthetized with isoflurane and placed in the abdominal position. Then, the inner mucosa of the bladder was slightly damaged with a modified intravenous catheter (24 gauge) by urethral catheterization. Subsequently, EJ cells were intravesically infused and incubated in the bladder for 1 to 2 hours. Next, the mouse urethra was clamped to prevent EJ cells from overflowing through the urethra.

### In vivo and ex vivo imaging of orthotopic bladder cancer xenograft model

After confirming tumor growth in the bladder, $Pep_{CXCR4}$ and bsGP (500 μM, 100 μl) were intravesically instilled and incubated in the bladder for 60 min for in vivo fluorescence imaging. Then, the mice were scanned with In Vivo Imaging System (IVIS) at predetermined time points (1, 4, 8, 12, 24, 48, and 72 hours) using an in vivo spectrum imaging system. In addition, the bladder of mice was exteriorized and imaged with IVIS to confirm the tumor-specific recognition of bsGP at 1 hour after intravesical infusion.

### Frozen tissue sections

Saline and bsGP (500 μM, 100 μl) were intravesically instilled into orthotopic EJ xenograft nude mice when the tumor size was approximately 200 $mm^3$. Then, tumor tissues were resected at 6 hours after instillation, followed by cutting into small pieces and fixing in optimal cutting temperature compound at 4°C overnight. After that, tumor tissues were cut into sections of 7 μm at −20°C. Subsequently, sections were sealed with saline and coverslips. Last, the slides were immediately observed with UltraVIEW VoX for imaging and analysis.

### Immunofluorescence and analysis

Orthotopic MB49-Luc bladder cancer mice were treated with saline, $Pep_{CXCR4}$ (500 μM, 100 μl), and bsGP (500 μM, 100 μl) once every 2 days for a total of five times. The immunofluorescence of whole tumor slices—including CXCR4, CD4, CD8, CD86, and CD206—was performed and analyzed by D. Liu and J.-F. Hao from the Core Facility for Protein Research, Institute of Boiphysics, Chinese Academy of Science.

### In vivo antitumor subcutaneous implantation efficiency

EJ xenograft mice were randomly divided into five groups ($n = 6$ per group) and intravenously injected with saline, $Pep_{CXCR4}$ (500 μM, 100 μl), plerixafor (100 μM, 100 μl), and bsGP (500 μM, 100 μl) through the tail vein once a day for a total of five times. Then, the mice were anesthetized with isoflurane to remove tumor tissue and divide it into homogeneous tiny sizes. Then, tiny tumor tissues were subcutaneously implanted into the right hind leg of female BALB/c nude mice (6 to 8 weeks, 16 to 18 g). The tumor volumes and body weight were measured with calipers every other day for analysis.

### In vivo antitumor efficiency in EJ xenograft mice

EJ xenograft mice were constructed by subcutaneously injecting 100 μl of ($5 \times 10^6$) cells into the right flank of BALB/c nude mice (6 to 8 weeks, 16 to 18 g). The mice were randomly divided into four groups ($n = 6$ per group). Afterward, the mice intravenously injected with saline, $Pep_{CXCR4}$ (500 μM, 100 μl), plerixafor (100 μM, 100 μl), and bsGP (500 μM, 100 μl) through the tail vein once a day for a total of five times. The tumor volumes and body weight were measured with calipers every other day for analysis.

### In vivo antitumor efficiency in MB49-Luc tumor-bearing mice

MB49-Luc tumor-bearing mice were constructed by subcutaneously injecting 100 μl of ($5 \times 10^6$) cells into the right flank of C57BL/6 mice (6 to 8 weeks, 16 to 18 g). The mice were randomly divided into six groups ($n = 6$ per group). Afterward, the mice intravenously injected with saline, prepared nano-GP, tri-Man, bsGP-uC, prepared nano-GP + tri-Man, or bsGP (500 μM, 100 μl) through the tail vein once a day for a total of five times. The tumor volumes and body weight were measured with calipers every other day for analysis.

### In vivo antitumor orthotopic implantation efficiency

Female C57BL/6 mice (6 to 8 weeks, 16 to 18 g) were anesthetized with isoflurane and placed in the abdominal position. Then, the inner mucosa of the bladder was slightly damaged with a modified intravenous catheter (24 gauge) by urethral catheterization to simulate the intraoperative wound. Afterward, MB49-Luc cells were intravesically instilled and incubated in the bladder. Next, the mouse urethra was clamped for 1 to 2 hours to prevent MB49-Luc cells from overflowing through the urethra. The mice were randomly divided into five groups ($n = 9$ per group). Afterward, saline, plerixafor (0.05 mg/ml, 100 μl), Dox (1 mg/ml, 100 μl), BCG (1 mg/ml, 100 μl), and bsGP (2 mg/ml, 100 μl) were intravesically instilled into the bladder for treatment once every 2 days for a total of five times. To monitor MB49-Luc cell implantation and progression in the bladder, mice were anesthetized and bioluminescently imaged with IVIS at 0, 10, 20, and 30 days after instillation for analysis.

### H&E staining and urinalysis

Histological analysis of major organs was harvested from mice after treatment with saline and bsGP (2 mg/ml, 100 μl) for 1 day by intravesical instillation and urinalysis of urine collected from mice after treatment with saline and bsGP (2 mg/ml, 100 μl) for 1, 7, and 14 days by Wuhan Servicebio Technology Co. Ltd.

### Statistical methods

Data were presented as the means ± SD. Statistical analysis of the data was performed with one-way analysis of variance (ANOVA), followed by post hoc Tukey's test. $^*P < 0.05$, $^{**}P < 0.01$, and $^{***}P < 0.001$. No effect size was predetermined. All the biochemical and biological experiments were performed in three replicates or more. No animals and/or data were excluded. The dosing groups were filled by randomly selecting from the same pool of animals for in vivo experiments. All experimental procedures and quantification of results—including injections, isolation of the tumors or organs, tissue histological analysis, and fluorescence-activated cell sorting—were done by two independent researchers.

## Supplementary Materials

**This PDF file includes:**

Figs. S1 to S34

View/request a protocol for this paper from *Bio-protocol*.

## REFERENCES AND NOTES


1. A. Cassell, B. Yunusa, M. Jalloh, M. M. Mbodji, A. Diallo, M. Ndoye, Y. Diallo, I. Labou, L. Niang, S. M. Gueye, Non-muscle invasive bladder cancer: A review of the current trend in Africa. *World J. Oncol.* **10**, 123–131 (2019).
2. M. Babjuk, M. Burger, E. M. Compérat, P. Gontero, A. H. Mostafid, J. Palou, B. W. G. van Rhijn, M. Rouprêt, S. F. Shariat, R. Sylvester, R. Zigeuner, O. Capoun, D. Cohen, J. L. D. Escrig, V. Hernández, B. Peyronnet, T. Seisen, V. Soukup, European Association of Urology guidelines on non-muscle-invasive bladder cancer (TaT1 and carcinoma in situ) - 2019 update. *Eur. Urol.* **76**, 639–657 (2019).
3. S. Daneshmand, A. Nazemi, Neoadjuvant chemotherapy in variant histology bladder cancer: Current evidence. *Eur. Urol. Focus* **6**, 639–641 (2020).
4. A. T. Lenis, P. M. Lec, K. Chamie, Bladder cancer: A review. *JAMA* **324**, 1980–1991 (2020).
5. D. Y. Hou, N.-Y. Zhang, M.-D. Wang, S.-X. Xu, Z.-J. Wang, X.-J. Hu, G.-T. Lv, J.-Q. Wang, X.-H. Wu, L. Wang, D.-B. Cheng, H. Wang, W. Xu, In situ constructed nano-drug depots through intracellular hydrolytic condensation for chemotherapy of bladder cancer. *Angew. Chem. Int. Ed.* **61**, e202116893 (2022).
6. M. Moussa, A. G. Papatsoris, A. Dellis, M. A. Chakra, W. Saad, Novel anticancer therapy in BCG unresponsive non-muscle-invasive bladder cancer. *Expert Rev. Anticancer Ther.* **20**, 965–983 (2020).
7. A. G. Robertson, C. S. Groeneveld, B. Jordan, X. Lin, K. A. McLaughlin, A. Das, L. A. Fall, D. Fantini, T. J. Taxter, L. S. Mogil, S. V. Lindskrog, L. Dyrskjøt, D. J. McConkey, R. S. Svatek, A. de Reyniès, M. A. A. Castro, J. J. Meeks, Identification of differential tumor subtypes of T1 bladder cancer. *Eur. Urol.* **78**, 533–537 (2020).
8. J. Taylor, E. Becher, G. D. Steinberg, Update on the guideline of guidelines: Non-muscle-invasive bladder cancer. *BJU Int.* **125**, 197–205 (2020).
9. R. T. Bryan, S. I. Collins, M. C. Daykin, M. P. Zeegers, K. K. Cheng, D. M. A. Wallace, G. M. Sole, Mechanisms of recurrence of Ta/T1 bladder cancer. *Ann. R. Coll. Surg. Engl.* **92**, 519–524 (2010).
10. K. Akagashi, H. Tanda, S. Kato, S. Ohnishi, H. Nakajima, A. Nanbu, T. Nitta, M. Koroku, Y. Sato, T. Hanzawa, Recurrence pattern for superficial bladder cancer. *Int. J. Urol.* **13**, 686–691 (2006).
11. Y. Lavin, S. Kobayashi, A. Leader, E.-A. D. Amir, N. Elefant, C. Bigenwald, R. Remark, R. Sweeney, C. D. Becker, J. H. Levine, K. Meinhof, A. Chow, S. Kim-Shulze, A. Wolf, C. Medaglia, H. Li, J. A. Rytlewski, R. O. Emerson, A. Solovyov, B. D. Greenbaum, C. Sanders, M. Vignali, M. B. Beasley, R. Flores, S. Gnjatic, D. Pe'er, A. Rahman, I. Amit, M. Merad, Innate immune landscape in early lung adenocarcinoma by paired single-cell analyses. *Cell* **169**, 750–765.e17 (2017).

12. M. Casanova-Acebes, E. Dalla, A. M. Leader, J. L. Berichel, J. Nikolic, B. M. Morales, M. Brown, C. Chang, L. Troncoso, S. T. Chen, A. Sastre-Perona, M. D. Park, A. Tabachnikova, M. Dhainaut, P. Hamon, B. Maier, C. M. Sawai, E. Agulló-Pascual, M. Schober, B. D. Brown, B. Reizis, T. Marron, E. Kenigsberg, C. Moussion, P. Benaroch, J. A. Aguirre-Ghiso, M. Merad, Tissue-resident macrophages provide a pro-tumorigenic niche to early NSCLC cells. *Nature* **595**, 578–584 (2021).
13. Z. Wei, X. Zhang, T. Yong, N. Bie, G. Zhan, X. Li, Q. Liang, J. Li, J. Yu, G. Huang, Y. Yan, Z. Zhang, B. Zhang, L. Gan, B. Huang, X. Yang, Boosting anti-PD-1 therapy with metformin-loaded macrophage-derived microparticles. *Nat. Commun.* **12**, 440 (2021).
14. K. Lei, A. Kurum, M. Kaynak, L. Bonati, Y. Han, V. Cencen, M. Gao, Y.-Q. Xie, Y. Guo, M. T. M. Hannebelle, Y. Wu, G. Zhou, M. Guo, G. E. Fantner, M. S. Sakar, L. Tang, Cancer-cell stiffening via cholesterol depletion enhances adoptive T-cell immunotherapy. *Nat. Biomed. Eng.* **5**, 1411–1425 (2021).
15. H. Xiao, Y. Guo, B. Li, X. Li, Y. Wang, S. Han, D. Cheng, X. Shuai, M2-like tumor-associated macrophage-targeted codelivery of STAT6 inhibitor and IKKβ siRNA induces M2-to-M1 repolarization for cancer immunotherapy with low immune side effects. *ACS Cent. Sci.* **6**, 1208–1222 (2020).
16. Y. Chao, L. Xu, C. Liang, L. Feng, J. Xu, Z. Dong, L. Tian, X. Yi, K. Yang, Z. Liu, Combined local immunostimulatory radioisotope therapy and systemic immune checkpoint blockade imparts potent antitumour responses. *Nat. Biomed. Eng.* **2**, 611–621 (2018).
17. B. A. Teicher, S. P. Fricker, CXCL12 (SDF-1)/CXCR4 pathway in cancer. *Clin. Cancer Res.* **16**, 2927–2931 (2010).
18. F. Balkwill, Cancer and the chemokine network. *Nat. Rev. Cancer.* **4**, 540–550 (2004).
19. J. S. Desgrosellier, D. A. Cheresh, Integrins in cancer: Biological implications and therapeutic opportunities. *Nat. Rev. Cancer.* **10**, 9–22 (2010).
20. A. Eisenhardt, U. Frey, M. Tack, D. Rosskopf, G. Lümmen, H. Rübben, W. Siffert, Expression analysis and potential functional role of the CXCR4 chemokine receptor in bladder cancer. *Eur. Urol.* **47**, 111–117 (2005).
21. M. Retz, S. S. Sidhu, E. Blaveri, S. C. Kerr, G. M. Dolganov, J. Lehmann, P. Carroll, J. Simko, F. M. Waldman, C. Basbaum, CXCR4 expression reflects tumor progression and regulates motility of bladder cancer cells. *Int. J. Cancer.* **114**, 182–189 (2005).
22. T. Zhang, F. Yang, W. Li, B. Liu, W. Li, Z. Chen, C. Wang, Suppression of the SDF-1/CXCR4/β-catenin axis contributes to bladder cancer cell growth inhibition in vitro and in vivo. *Oncol. Rep.* **40**, 1666–1674 (2018).
23. C. Feig, J. O. Jones, M. Kraman, R. J. B. Wells, A. Deonarine, D. S. Chan, C. M. Connell, E. W. Roberts, Q. Zhao, O. L. Caballero, S. A. Teichmann, T. Janowitz, D. I. Jodrell, D. A. Tuveson, D. T. Fearon, Targeting CXCL12 from FAP-expressing carcinoma-associated fibroblasts synergizes with anti-PD-L1 immunotherapy in pancreatic cancer. *Proc. Natl. Acad. Sci. U.S.A.* **110**, 20212–20217 (2013).
24. K. Jung, T. Heishi, J. Incio, Y. Huang, E. Y. Beech, M. Pinter, W. W. Ho, K. Kawaguchi, N. N. Rahbari, E. Chung, J. K. Kim, J. W. Clark, C. G. Willett, S. H. Yun, A. D. Luster, T. P. Padera, R. K. Jain, D. Fukumura, Targeting CXCR4-dependent immunosuppressive $Ly6C^{low}$ monocytes improves antiangiogenic therapy in colorectal cancer. *Proc. Natl. Acad. Sci. U.S.A.* **114**, 10455–10460 (2017).
25. L. Cassetta, J. W. Pollard, Targeting macrophages: Therapeutic approaches in cancer. *Nat. Rev. Drug Discov.* **17**, 887–904 (2018).
26. V. K. Chaturvedi, A. Singh, V. K. Singh, M. P. Singh, Cancer nanotechnology: A new revolution for cancer diagnosis and therapy. *Curr. Drug Metab.* **20**, 416–429 (2019).
27. D.-Y. Hou, W.-Y. Xiao, J.-Q. Wang, M. Yaseen, Z.-J. Wang, Y. Fei, M.-D. Wang, L. Wang, H. Wang, X. Shi, M.-M. Cai, H.-T. Feng, W. Xu, L.-L. Li, OGA activated glycopeptide-based nano-activator to activate PKM2 tetramerization for switching catabolic pathways and sensitizing chemotherapy resistance. *Biomaterials* **284**, 121523 (2022).
28. C. Jiang, H. Cai, X. Peng, P. Zhang, X. Wu, R. Tian, Targeted imaging of tumor-associated macrophages by cyanine 7-labeled mannose in xenograft tumors. *Mol. Imaging.* **16**, 1536012116689499 (2017).
29. A. Egorova, A. Kiselev, M. Hakli, M. Ruponen, V. Baranov, A. Urtti, Chemokine-derived peptides as carriers for gene delivery to CXCR4 expressing cells. *J. Gene Med.* **11**, 772–781 (2009).
30. H.-W. An, D. Hou, R. Zheng, M.-D. Wang, X.-Z. Zeng, W.-Y. Xiao, T.-D. Yan, J.-Q. Wang, C.-H. Zhao, L.-M. Cheng, J.-M. Zhang, L. Wang, Z.-Q. Wang, H. Wang, W. Xu, A near-infrared peptide probe with tumor-specific excretion-retarded effect for image-guided surgery of renal cell carcinoma. *ACS Nano* **14**, 927–936 (2020).
31. H.-W. An, L.-L. Li, Y. Wang, Z. Wang, D. Hou, Y.-X. Lin, S.-L. Qiao, M.-D. Wang, C. Yang, Y. Cong, Y. Ma, X.-X. Zhao, Q. Cai, W.-T. Chen, C.-Q. Lu, W. Xu, H. Wang, Y. Zhao, A tumour-selective cascade activatable self-detained system for drug delivery and cancer imaging. *Nat. Commun.* **10**, 4861 (2019).
32. D. Y. Hou, M.-D. Wang, X.-J. Hu, Z.-J. Wang, N.-Y. Zhang, G.-T. Lv, J.-Q. Wang, X.-H. Wu, L. Wang, H. Wang, W. Xu, An activated excretion-retarded tumor imaging strategy towards metabolic organs. *Bioact. Mater.* **14**, 110–119 (2021).
33. R. Seiler, G. N. Thalmann, A. Fleischmann, MMP-2 and MMP-9 in lymph-node-positive bladder cancer. *J. Clin. Pathol.* **64**, 1078–1082 (2011).
34. Z. Song, H. Fu, R. Wang, L. A. Pacheco, X. Wang, Y. Lin, J. Cheng, Secondary structures in synthetic polypeptides from *N*-carboxyanhydrides: Design, modulation, association, and material applications. *Chem. Soc. Rev.* **47**, 7401–7425 (2018).
35. J. J. Lundquist, E. J. Toone, The cluster glycoside effect. *Chem. Rev.* **102**, 555–578 (2002).
36. D. B. Cheng, X.-H. Zhang, Y.-J. Gao, L. Ji, D. Hou, Z. Wang, W. Xu, Z.-Y. Qiao, H. Wang, Endogenous reactive oxygen species-triggered morphology transformation for enhanced cooperative interaction with mitochondria. *J. Am. Chem. Soc.* **141**, 7235–7239 (2019).
37. L. Zhang, D. Jing, N. Jiang, T. Rojalin, C. M. Baehr, D. Zhang, W. Xiao, Y. Wu, Z. Cong, J. J. Li, Y. Li, L. Wang, K. S. Lam, Transformable peptide nanoparticles arrest HER2 signalling and cause cancer cell death in vivo. *Nat. Nanotechnol.* **15**, 145–153 (2020).
38. H. Wang, Z. Fenga, B. Xu, Bioinspired assembly of small molecules in cell milieu. *Chem. Soc. Rev.* **46**, 2421–2436 (2017).
39. S. Lundgren, P. Micke, J. Elebro, M. Heby, I. Hrynchyk, B. Nodin, K. Leandersson, A. Mezheyeuski, K. Jirström, Topographical distribution and spatial interactions of innate and semi-innate immune cells in pancreatic and other periampullary adenocarcinoma. *Front. Immunol.* **11**, 558169 (2020).


**Acknowledgments:** We thank the State Key Laboratory of Natural and Biomimetic Drugs, School of Pharmaceutical Sciences, Peking University, and W.-Z. Li for help and support in fluorescent imaging during the coronavirus disease 2019 pandemic. **Funding:** This work was supported by National Key R&D Program of China (2020YFA0210800), National Natural Science Foundation of China (51725302, 52003270, and 11621505), National Key R&D Program of China (2018YFE0205403), and Regional Key Project of National Natural Science Foundation of China (U20A20385). **Author contributions:** H.-W.A., D.-Y.H., W.X., Y.Z., and H.W. conceived the project. H.-W.A., J.Y., R.Z., and M.-D.W. performed all the compound syntheses and characterizations. J.Y., D.-Y.H., and H.-W. A. collected enzymatic reactions and carried out cell imaging. D.-Y.H., Z.-Q.W., Z.-J.W., W.X., and H.-W.A. set up the animal model. D.-Y.H., Z.-J.W., and X.-J.H. performed the in vivo studies, and D.-Y.H. analyzed the data. D.-Y.H., Z.-J.W., and X.-J.H. performed the flow cytometer studies and analyzed the data. H.-W.A., D.-Y.H., D.L., and J.-F. H. performed the immunofluorescence and data analysis of tissue sections. All authors discussed the results and commented on the manuscript. H.-W.A., D.-Y.H., W.X., Y.Z., and H.W. cowrote the paper. **Competing interests:** The authors declare that they have no competing interests. **Data and materials availability:** All data needed to evaluate the conclusions in the paper are present in the paper and/or the Supplementary Materials.

Submitted 6 May 2022
Accepted 1 February 2023
Published 1 March 2023
10.1126/sciadv.abq8225